



Universiteit
Leiden
The Netherlands

The composition and thermal properties of a cool core lacking a brightest cluster galaxy

Su, Y.; Combes, F.; Olivares, V.; Castignani, G.; Torne, P.; Weeren, R.J. van

Citation

Su, Y., Combes, F., Olivares, V., Castignani, G., Torne, P., & Weeren, R. J. van. (2023). The composition and thermal properties of a cool core lacking a brightest cluster galaxy. *Monthly Notices Of The Royal Astronomical Society*, 526(4), 6052-6058.
doi:10.1093/mnras/stad3172

Version: Publisher's Version
License: [Creative Commons CC BY 4.0 license](https://creativecommons.org/licenses/by/4.0/)
Downloaded from: <https://hdl.handle.net/1887/3719306>

Note: To cite this publication please use the final published version (if applicable).

The composition and thermal properties of a cool core lacking a brightest cluster galaxy

Yuanyuan Su ¹★, Francoise Combes ², Valeria Olivares¹, Gianluca Castignani ^{3,4}, Pablo Torne ⁵ and Reinout van Weeren ⁶

¹Department of Physics and Astronomy, University of Kentucky, 505 Rose Street, Lexington, KY 40506, USA

²Observatoire de Paris, LERMA, Collège de France, CNRS, Sorbonne University, PSL University, F-75014 Paris, France

³Dipartimento di Fisica e Astronomia ‘Augusto Righi’, Alma Mater Studiorum Università di Bologna, Via Gobetti 93/2, I-40129 Bologna, Italy

⁴INAF – Osservatorio di Astrofisica e Scienza dello Spazio di Bologna, via Gobetti 93/3, I-40129, Bologna, Italy

⁵Institut de Radioastronomie Millimétrique, Avda. Divina Pastora 7, Local 20, E-18012 Granada, Spain

⁶Leiden Observatory, Leiden University, PO Box 9513, NL-2300 RA Leiden, the Netherlands

Accepted 2023 October 2. Received 2023 October 1; in original form 2023 June 6

ABSTRACT

We present a multiwavelength observation of a cool core that does not appear to be associated with any galaxy, in a nearby cluster, Abell 1142. Its X-ray surface brightness peak of ≈ 2 keV is cooler than the ambient intracluster gas of $\gtrsim 3$ keV, and is offset from its brightest cluster galaxy (BCG) by 80 kpc in projection, representing the largest known cool core – BCG separation. This BCG-less cool core allows us to measure the metallicity of a cluster centre with a much-reduced contribution from the interstellar medium (ISM) of the BCG. *XMM–Newton* observation reveals a prominent Fe abundance peak of $1.07_{-0.15}^{+0.16} Z_{\odot}$ and an α /Fe abundance ratio close to the solar ratio, fully consistent with those found at the centres of typical cool core clusters. This finding hints that BCGs play a limited role in enriching the cluster centres. However, the discussion remains open, given that the α /Fe abundance ratios of the orphan cool core and the BCG ISM are not significantly different. Abell 1142 may have experienced a major merger more than 100 Myr ago, which has dissociated its cool core from the BCG. This implies that the Fe abundance peak in cool core clusters can be resilient to cluster mergers. Our recent Institut de Radio Astronomie Millimétrique 30-m observation did not detect any CO emission at its X-ray peak and we find no evidence for massive runaway cooling in the absence of recent active galactic nucleus feedback. The lack of a galaxy may contribute to an inefficient conversion of the ionized warm gas to the cold molecular gas.

Key words: galaxies: clusters: individual Abell 1142 – galaxies: clusters: intracluster medium – X-rays: galaxies: clusters.

1 INTRODUCTION

The intracluster medium (ICM), constituting 90 per cent of the cluster baryons, is the reservoir of nearly all metals that have ever been produced by member galaxies. The ICM is therefore an ideal and unique laboratory to study the enrichment process of the Universe as well as to constrain models of supernova nucleosynthesis. The bulk of the ICM of various different clusters tends to have Fe metallicities consistent with a constant value of 0.3 solar (Urban et al. 2017), which supports early enrichment: chemical elements were deposited and mixed into the intergalactic medium (IGM) before clusters formed (Werner et al. 2013; Simionescu et al. 2015; Urban et al. 2017). However, the uncertainty of these measurements is greater than 20 per cent and the measurements were performed with a spatial resolution of a few hundred kpc, therefore a non-uniform composition cannot be ruled out. Furthermore, the observed Fe mass in the ICM, when integrated to large radii, far exceeds what can be

produced by the visible stellar population (E Blackwell, Bregman & Snowden 2021; Ghizzardi et al. 2021; Sarkar et al. 2022), which is difficult to reconcile with the prevailing enrichment model.

Another outstanding puzzle has arisen in the study of cluster centres. Fe metallicity peaks sharply towards cluster centres in cool core (CC) clusters, which is generally considered to be due to the metals accumulated in the interstellar medium (ISM) of the brightest cluster galaxy (BCG). The composition of the gas at the cluster centres, as inferred from the abundance ratios, is consistent with that of our Solar system (e.g. Mernier et al. 2018). The enrichment of the IGM, before the formation of galaxy clusters, is likely to have a supersolar α /Fe ratio, due to the relatively short star formation time-scales for core collapse supernova (SNcc). The stellar mass-loss from the BCG may have enriched cluster centres with additional Type Ia supernova (SNIa) yields, after the gravitational collapse of clusters, as it would take a much longer time to form white dwarfs. The observed abundance pattern at the cluster centres would require these two sources of metals to compensate for each other to produce the solar ratios for nearly all clusters studied so far. This striking coincidence has been coined as the ‘ICM solar composition paradox’

* E-mail: ysu262@g.uky.edu

(Mernier et al. 2018). Fe metallicity also increases towards the centre of non-cool core (NCC) clusters but with a much smaller gradient, which has been attributed to mergers disrupting the cluster central metallicity peak (Leccardi, Rossetti & Molendi 2010).

Cluster CCs also feature a sharp X-ray surface brightness peak, where the gas is expected to cool to below 100 K and rapidly form stars at rates of $100\text{--}1000 M_{\odot} \text{ yr}^{-1}$, exceeding the observed star formation rates by orders of magnitudes (Peterson et al. 2003). Mechanical feedback from the active galactic nucleus (AGN) of the BCG is likely preventing this hot ICM from cooling, as revealed by the ubiquitous X-ray cavities at cluster CCs (see Fabian 2012 for a review). Recent observations of a high redshift ($z = 1.7$) cluster, SpARCS1049+56, have added new insight into this picture (Webb et al. 2017; Castignani, Combes & Salomé 2020; Hlavacek-Larrondo et al. 2020). Stars are forming at its centre, at an enormous rate of $860 \pm 140 M_{\odot} \text{ yr}^{-1}$, in association with a large reservoir of molecular gas of $1.1 \times 10^{11} M_{\odot}$. The cold gas and star formation can in principle be fueled by massive, runaway cooling of the intracluster gas, perhaps precisely due to the absence of AGN feedback, as its X-ray peak is offset from the BCG. A relevant object was discovered in the nearby Universe – ‘an orphan cloud’ serendipitously detected on the outskirts of Abell 1367 (Ge et al. 2021): an isolated cloud (no optical counterpart) with an effective radius of 30 kpc, detected in X-rays, H α , and CO, which may have been stripped off from an unidentified member galaxy (Jáchym et al. 2022).

Abell 1142 is a nearby galaxy cluster that has connections to both SpARCS1049+56 and the orphan cloud. It is undergoing a major merger and the spectroscopically confirmed member galaxies in Abell 1142 display a nearly bimodal redshift distribution peaking at $z = 0.0325$ and 0.0375 , respectively (Fig. 1; also see Su et al. 2016). *Chandra* Advanced CCD Imaging Spectrometer (ACIS)-S observation reveals that its X-ray peak is 80 kpc east of the BCG, IC 664, a massive elliptical galaxy at $z = 0.0338$ (Su et al. 2016). This X-ray emission is unlikely to be a background cluster as this field is covered by Sloan Digital Sky Survey (SDSS; Kollmeier et al. 2019) and there is no known optical counterpart at higher redshift (Su et al. 2016). Abell 1142 presents the largest known offset between a cluster CC and the BCG¹. It provides a valuable opportunity, in the nearby Universe, to unambiguously measure the metallicity of a cluster CC itself, with a minimized impact of the ISM of the BCG, and to test the role of the AGN feedback at cluster centres. Previous *Chandra* observations reveal a temperature of 2 keV and a metal abundance of $1 Z_{\odot}$ at the CC, cooler and more metal rich than the ambient ICM of 3 keV and $0.2 Z_{\odot}$. Notably, its metallicity profile is consistent with that derived for typical cool-core clusters and deviates from that of NCC clusters (see Su et al. 2016).

This paper presents follow-up multiwavelength observations of Abell 1142, using *XMM-Newton* and Institut de Radio Astronomie Millimétrique (IRAM) 30-m, to study the two-dimensional distribution of its gas properties and search for multiphase gas associated with the orphan CC. The paper is structured as follows. The data preparation and methods are presented in Section 2. The results of the metallicity and multiple phase gas measurements are shown in Section 3. Our findings are discussed in Section 4 and summarized in Section 5. We use NASA/IPAC Extragalactic Database² to estimate the luminosity distance of 153.9 Mpc (1 arcsec = 0.697 kpc) at

$z = 0.035$ for Abell 1142, by adopting a cosmology of $H_0 = 70 \text{ km s}^{-1} \text{ Mpc}^{-1}$, $\Omega_{\Lambda} = 0.7$, and $\Omega_{\text{m}} = 0.3$. We assume a solar abundance table of Asplund et al. (2009) throughout this paper. All uncertainties are reported at 1σ confidence level.

2 OBSERVATIONS AND DATA REDUCTION

2.1 XMM-Newton

Abell 1142 was observed with *XMM-Newton* in 2016 for an effective time of 100 ksec (Fig. 2 and Table 1). Data reduction was performed with the Science Analysis System version `xmmsas_20210317_1624-19.1.0`. Observation Data Files (ODF) were processed using `emchain` and `epchain`. Soft flares from MOS and pn data were filtered using `mos-filter` and `pn-filter`, respectively. Only FLAG = 0 and PATTERN < =12 event files are included for MOS data and only FLAG = 0 and PATTERN < =4 event files are included for pn data. Out-of-time pn events were also removed. Point sources were detected by `edetect_chain`, confirmed by eye, and removed from spectral analysis.

We extracted spectra from an annulus of 7.4–11.9 arcmin in radius to determine the astrophysical X-ray background (AXB) as well as the non-X-ray background (NXB) simultaneously. To better constrain the level of the local bubble and Milky Way foregrounds, we also included a ROSAT All Sky Survey (RASS) spectrum extracted from an annulus centred on but beyond the field of view of the *XMM-Newton* pointing. The spectral fit was restricted to the 0.3–10.0 keV energy band for *XMM-Newton* and 0.1–2.4 keV for RASS. We use `phabs*(powcxb + apecmw) + apecLB` to model the AXB. A power-law `powcxb` with index $\Gamma = 1.41$ represents the cosmic X-ray background (CXB), a thermal emission `apecLB` with a temperature of 0.08 keV for local bubble emission, and another `apecmw` with a temperature of 0.2 keV was for the Milky Way foreground. Metal abundance and redshift were fixed at 1 and 0, respectively, for `apecLB` and `apecmw`. The aforementioned annulus is chosen as far from the cluster centre as possible, while still ensuring enough photons to constrain the background components. Still, it may contain ICM emission. Therefore, we include `apecICM` to model the ICM component and allow its temperature, abundance, and normalization free to vary. The NXB model includes a set of Gaussian lines and a broken power law with $E_{\text{break}} = 3 \text{ keV}$ to model a set of fluorescent instrumental lines and a continuum spectrum for each MOS and pn detector (see the Appendix in Su et al. 2017 for details). The NXB model was not folded through the auxiliary response files. We inspect the ratio of area-corrected count rates in the 6–12 keV energy band within the field of view (excluding the central 10 arcmin) and in the unexposed corners. Our observations are not contaminated by the soft proton flare.

2.2 IRAM 30-m

We performed an observation of Abell 1142 with the IRAM 30-m telescope operated by the Institut de Radio Astronomie Millimétrique (IRAM) at Pico Veleta, Spain. The observation was carried out with the WSW mode, targeting a few positions³ mainly near the X-ray centroid as shown in Fig. 2. The observation (E01-22) was carried

¹Galaxy clusters known to have >80 kpc offset between CC and BCG are found to be binary or triple clusters, for which the CC is occupied by the brightest galaxy in the subcluster De Propriis et al. (2021).

²<http://ned.ipac.caltech.edu>

³These positions are chosen based on a tentative detection of extended CO(1-0) emission from a previous IRAM 30-m observation using on-the-fly mapping mode (030-22). But we now consider this ‘detection’ flawed by baseline ripples due to poor weather.

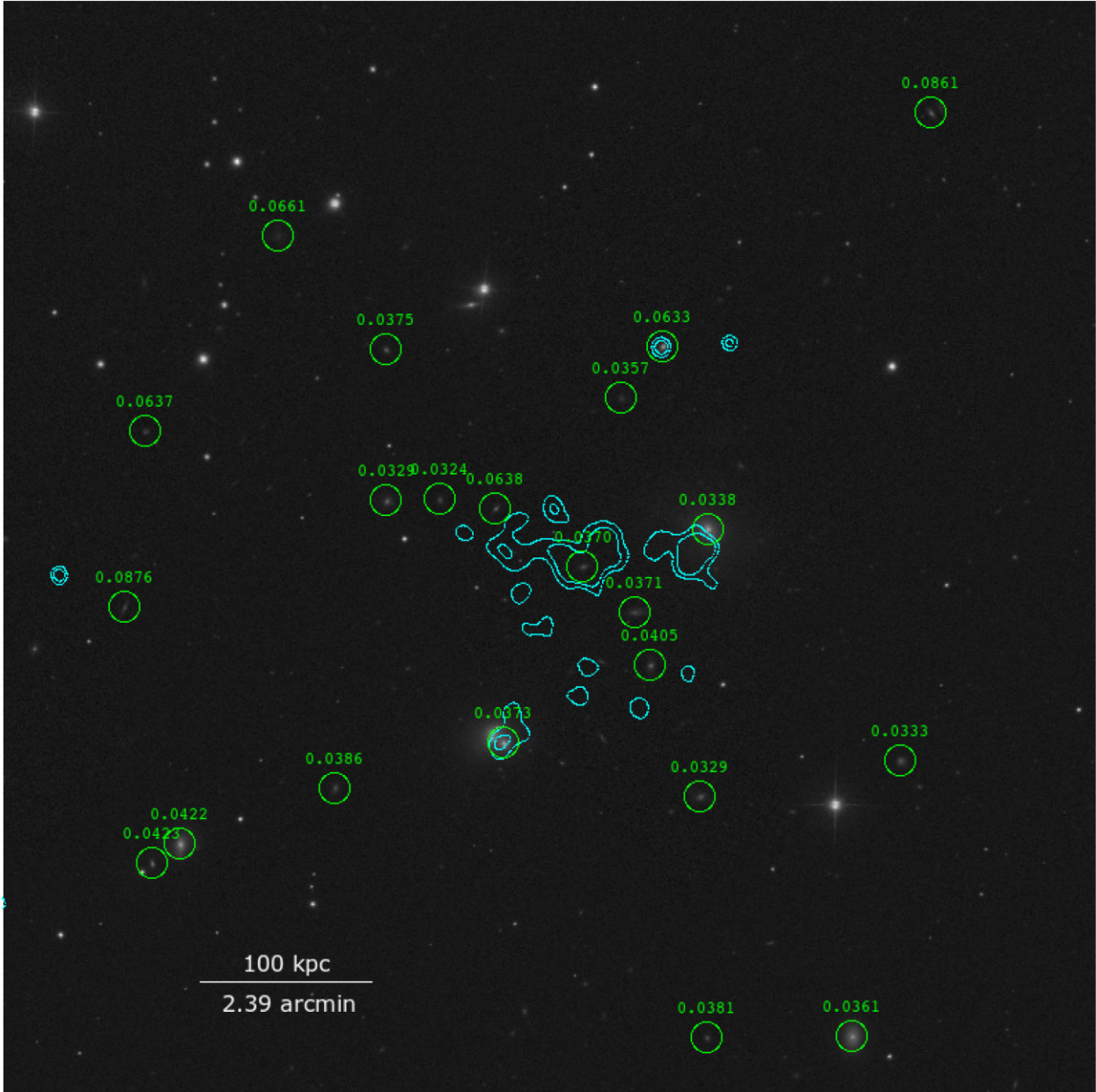


Figure 1. SDSS image of Abell 1142. The cyan contours overlaid trace the *Chandra* X-ray surface brightness as presented in Su et al. (2016). Spectroscopically confirmed galaxies are circled with their spectroscopic redshifts labelled.

out from 2023 February 21 to 2023 February 22 (Table 1). The Eight MIXer Receiver (EMIR) receiver was used to simultaneously observe at the frequencies of the CO(1-0) and CO(2-1) transitions. The Fast Fourier Transform Spectrometers (FTS) spectrometer and the Wideband Line Multiple Autocorrelator (WILMA) autocorrelator were connected to both receivers. 1055+018 and IRC+10216 were used as flux calibrators.

The half power beam width of the IRAM 30-m is ~ 22 arcsec for CO(1-0) and ~ 11 arcsec for CO(2-1). Data reduction was performed using CLASS from the GILDAS⁴ software package. The corrected antenna temperatures, T_{a^*} , were converted to the brightness temperature of the main beam by $T_{mb} = T_{a^*} F_{\text{eff}}/\eta_{mb}$. The main

beam efficiency is $\eta_{mb} = 0.78$ and 0.61 for 110 GHz and 220 GHz, respectively, and the forward efficiencies $F_{\text{eff}} = 0.94$ and 0.93 , respectively. The flux density is converted from the main beam antenna temperature by the ratio $\sim 5 \text{ Jy K}^{-1}$ both for CO(1-0) and CO(2-1) transitions. However, we did not detect any emission line associated with the CO(1-0) or CO(2-1) transition.

3 RESULTS

3.1 Metallicity

We produce adaptively binned temperature and metallicity maps of Abell 1142 using *XMM-Newton* observations. A square region with a side length of 7.56 arcmin was chosen covering the Abell 1142 centroid, major member galaxies, and their surroundings. The region

⁴<http://www.iram.fr/IRAMFR/GILDAS>

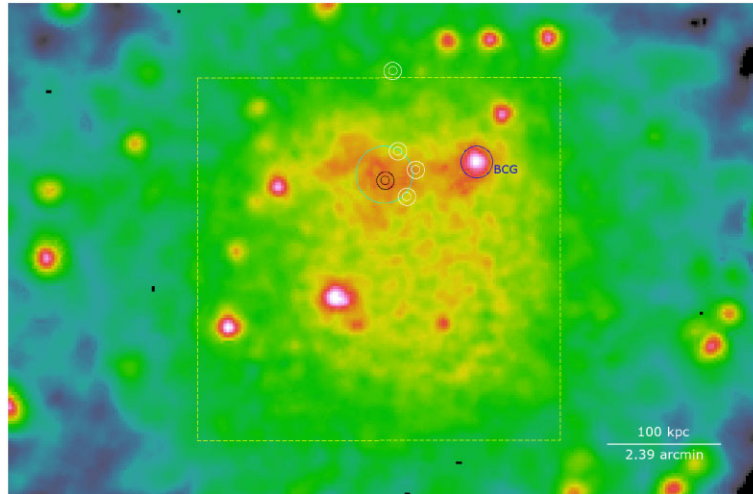


Figure 2. Particle background subtracted and vignetting corrected *XMM-Newton* EPIC image of the Abell 1142 galaxy cluster in the energy band of 0.7–1.3 keV. The positions of the IRAM 30-m wobbler switching (WSW) observations are marked in annuli (the inner circle and the outer circle correspond to the beam size of the 230 GHz and 115 GHz observations). The regions used to measure the abundance ratio of the cluster centre and the BCG are marked in cyan and blue circles. The yellow dashed square region marks the field of Fig. 3.

Table 1. List of *XMM-Newton* and IRAM 30-m observations presented in this paper.

Instrument	Observation	Date	Effective exposure	PI
<i>XMM-Newton</i> EPIC	0782330101	Jun 2016	37 (MOS), 20 (pn) ksec	Y. Su
<i>XMM-Newton</i> EPIC	0782330301	Jun 2016	100 (MOS), 82 (pn) ksec	Y. Su
IRAM 30-m	E01-22	Feb 2023	11 h	Y. Su

was divided into a 14×14 grid of pixels. We extract a spectrum from a circular region centred on each pixel. Its radius is chosen adaptively to collect at least 500 net counts. Response files were produced for each spectrum. We apply the same model used for the annulus region to model the AXB, NXB, and ICM components (see Section 2.1) of each region. The parameters of the AXB model and most parameters of the NXB model are fixed to those determined earlier. We allow the normalization of the fluorescent instrumental lines at 1.49 keV and 1.75 keV free to vary for MOS and that of the 1.48 keV line free to vary for pn. We first fix the ICM metallicity at $0.3 Z_{\odot}$ and obtain a temperature map as shown in Fig. 3-left. We then allow metallicity free to vary to obtain a metallicity map as shown in Fig. 3-right. The 2D spatial distribution of its gas properties demonstrates that the orphan CC is cooler than the surrounding ICM. The metallicity peaks around the orphan CC, approaching $1 Z_{\odot}$, in contrast to the ambient ICM outside the CC of $0.2 Z_{\odot}$. The spectrum extraction regions, with radii ranging from 0.5 arcmin at the centre to 1.3 arcmin at the outskirts, are chosen through adaptive-binning and overlap with adjacent regions; the actual temperature and metal abundance contrast are likely to be more pronounced.

To constrain the metallicity of the CC, we extract a spectrum from a circular region centred on the X-ray peak with a radius of 25 kpc (cyan circle in Fig. 2). The spectrum was fit to a two-temperature thermal `phabs*(vapec + vapec)` model (along with multiple background components as described in the previous paragraph), in which all the α elements (O, Ne, S, Si, Al, Ca), mainly the products of SNcc, are linked together, while Fe and Ni, mainly synthesized in SNIa, are linked together. One of the two temperatures is free to vary, for which we obtain a best-fitting temperature of $1.11^{+0.10}_{-0.08}$ keV, while the other temperature is fixed at 3 keV (the temperature at the outer atmosphere of the ICM as shown in Fig. 3-left). We obtain

a best-fitting Fe abundance of $1.07^{+0.16}_{-0.15} Z_{\odot}$ and an α/Fe ratio of $0.95^{+0.28}_{-0.27}$ the Solar ratio, consistent with the Fe abundance peak and abundance ratios measured for typical CC clusters. We performed a similar spectral analysis for a circular region of $r < 14$ kpc centred on the BCG using exactly the same model⁵. We obtain a best-fitting Fe abundance of $0.78^{+0.21}_{-0.16} Z_{\odot}$ and an α/Fe ratio of 0.65 ± 0.28 the Solar ratio. This latter measurement, presumably more representative of the BCG ISM metallicity, is more dominated by the SNIa yields, although consistent within the uncertainties with the composition observed for the orphan CC.

3.2 Cold molecular gas

To capture a potential multiphase gas near the X-ray centroid, we performed an IRAM 30-m observation of Abell 1142, using the WSW mode to obtain a ripple-free baseline and targeting on both CO(1-0) and CO(2-1) transitions. We observed a few positions mainly within the orphan core, and we did not detect any CO emission line with a clean baseline. A new issue was raised a few days before the observation. The maximum throw had been limited to 30 arcsec, with no fix on the horizon. If the emission is extended, the signal

⁵Using the point source detection tool `wavdetect`, we identified a point-like source at the very centre of the BCG from the existing *Chandra* ACIS-S observation. We extracted the spectrum from this source with a circular region of $r < 1.8$ arcsec and used an annulus region of $1.8 \text{ arcsec} < r < 2.7 \text{ arcsec}$ as the local background. The spectrum was fit to an absorbed power-law model, for which we obtain a best-fitting photon index of 4.1 ± 0.5 , which is too soft to be a nuclear source and is likely to be thermal emission. Therefore, we did not include an additional power-law component in the spectral analysis of the BCG.

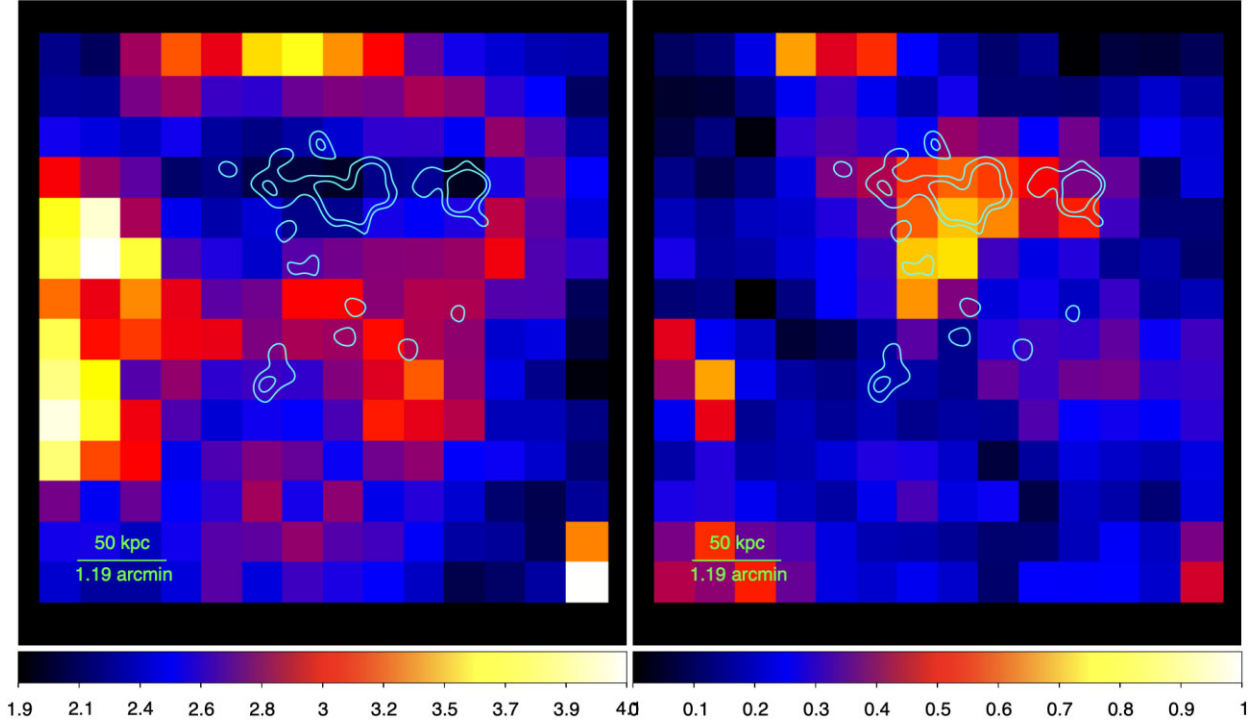


Figure 3. Left: temperature map in units of keV obtained with *XMM-Newton*. Right: metallicity map in units of solar abundance obtained with *XMM-Newton*. Overlaid is the cyan contour tracing the *Chandra* X-ray surface brightness as presented in Su et al. (2016).

would be reduced due to the limited maximum throw. Based on the WSW observation at its X-ray peak (black annulus in Fig. 2), we set 3σ upper limits of 1.1 Jy km s^{-1} and 1.7 Jy km s^{-1} on the CO(1-0) and CO(2-1) emission lines, respectively, at a velocity resolution of 300 km s^{-1} . We calculate the upper limit on the CO luminosity from the standard conversion of

$$L'_{\text{CO}} = 3.25 \times 10^7 S_{\text{CO}} \Delta v \nu_{\text{obs}}^{-2} D_L^2 (1+z)^{-3} \text{ K km s}^{-1} \text{ pc}^2 \quad (1)$$

where $S_{\text{CO}} \Delta v$ is the CO velocity integrated flux for an emission line in Jy km s^{-1} , ν_{obs} is the observed frequency in GHz, and D_L is the luminosity distance in Mpc. The molecular gas mass in H_2 is estimated from $M_{\text{H}_2} [M_{\odot}] = \alpha_{\text{CO}} L'_{\text{CO}} [\text{K km s}^{-1} \text{ pc}^2]$, where we choose $\alpha_{\text{CO}} = 4.6 M_{\odot} / (\text{K km s}^{-1} \text{ pc}^2)$ as in our Galaxy (Solomon & Barrett 1991). This CO-H₂ conversion only applies to CO(1-0). A factor of R_{1J} must be added for the CO(J, J-1) transitions and in this case we take $R_{12} = 1.2$ for CO(2-1) (Tacconi et al. 2018). We obtain 3σ upper limits on M_{H_2} of $2.8 \times 10^8 M_{\odot}$ and $1.4 \times 10^8 M_{\odot}$ based on CO(1-0) and CO(2-1) measurements, respectively.

4 DISCUSSIONS

4.1 Enrichment process of the ICM

Extensive *XMM-Newton* observations of the centres of CC clusters, i.e. the CHEMical Enrichment RGS cluster Sample (CHEERS) catalogue of X-ray bright galaxy groups, clusters, and elliptical galaxies, have revealed that the ratios of multiple elements relative to Fe (X/Fe) are consistent with the chemical composition of our Solar system, and in excellent agreement with the measurement of the centre of the Perseus cluster using the microcalorimetre onboard Hitomi (Mernier et al. 2018).

The abundance ratios outside cluster cores have been observed with *Suzaku* for only a few clusters (Simionescu et al. 2015; Sarkar et al. 2022). However, unlike cluster centres, agreement on abundance

ratios of cluster outskirts has not been reached. Simionescu et al. (2015) have presented the results of a *Suzaku* key project on the nearest galaxy cluster, Virgo. Abundance ratios of Si/Fe, Mg/Fe, and S/Fe out to its virial radius have been reported, which are generally consistent with the Solar value. Recently, Sarkar et al. (2022) presented the O/Fe, Si/Fe, Mg/Fe, and S/Fe ratios for 4 low mass clusters out to their virial radii. The α/Fe ratios are found to be consistent with Solar abundances at their centres, but increase outside the cluster centres and reach $2\times$ the Solar value. Interestingly, this latter measurement, with α/Fe profiles increasing with radius, is fully consistent with the prediction of the IllustrisTNG cosmological simulation (Sarkar et al. 2022).

If α/Fe is found to be uniform in the ICM, from the centres to the outskirts, it would imply that the metals throughout the ICM have the same origin, likely from an epoch before the gravitational collapse of the clusters. If the compositions of the cluster outskirts deviate from those of the centres, it favours different enrichment channels. For example, the cluster outskirts may have been enriched at an earlier epoch (SNcc dominated), while the centres may have been enriched later on by the stellar mass-loss of the BCG (SNIa dominated), as predicted by IllustrisTNG.

In this study, we performed abundance measurement for a cluster centre, for the first time, without the immediate influence of the innermost atmosphere of the BCG – minimizing the contribution of BCG to the metallicity of the cluster centres. We cannot individually constrain X/Fe for each element. Instead we linked all the elements that are mainly synthesized in core collapse supernovae. The best-fitting α/Fe ratio of about the Solar value as well as an abundance peak of Fe of ~ 1 solar for the BCG-less CC in Abell 1142 are fully consistent with those found for typical CC with a BCG. This finding hints at a limited role of the BCG in enriching the cluster centres and producing a solar-like composition.

A robust comparison of the composition of cluster centres and outskirts would be the key to understanding the enrichment process

of the ICM. Both of these aforementioned Suzaku studies have sizable uncertainties for measuring cluster outskirts. Observations with future X-ray instruments such as the Line Emission Mapper X-ray Probe (Kraft et al. 2022) may allow us to convincingly measure the abundance ratios of the cluster outskirts.

4.2 The impact of mergers on metal-rich cool cores

The dichotomy of CC and NCC clusters has been a lasting puzzle in the study of cluster formation and evolution. The Fe abundance peak in NCC clusters is not nearly as pronounced as in CC clusters, as an anticorrelation between entropy and metallicity has been observed at cluster centres (Leccardi, Rossetti & Molendi 2010). A CC is considered a natural outcome of radiative cooling, and major mergers may have disrupted cluster CCs and created NCC clusters (Su et al. 2020). This prevailing theory was challenged by a recent joint *Chandra* and SPT analysis of 67 galaxy clusters at $0.3 < z < 1.3$, revealing that the fraction of CC clusters has not evolved over the past 9 Gyr (Ruppin et al. 2021). This would require CC clusters to be converted to NCC clusters by mergers, at exactly the same rate as NCC clusters transform to CC clusters by cooling, at every redshift interval, seriously questioning the role of mergers in destroying cluster CCs (Olivares et al. 2022).

In this study, we measure an Fe abundance peak of $\sim 1.0 Z_{\odot}$ for the central $r < 25$ kpc of the orphan CC in Abell 1142. This CC has clearly been through a recent major merger, as indicated by the bimodal velocity distribution of the member galaxies and the large offset between the X-ray peak and BCG. The prominent Fe abundance peak of the orphan CC implies that the Fe peak of CC clusters may be able to survive some mergers.

4.3 The lack of cold gas detection in the orphan cool core

We did not detect cold molecular gas at the X-ray peak of Abell 1142 (black annulus in Fig. 2). We derive the cooling rate of $1.2 M_{\odot} \text{ yr}^{-1}$ for the orphan core, using

$$M_{\text{cf}} = \frac{2m_{\mu}m_{\text{p}}L_{\text{X}}}{5kT}, \quad (2)$$

where $L_{\text{X}} = 3 \times 10^{41} \text{ erg s}^{-1}$ is the bolometric luminosity measured with *XMM-Newton* and we assume a temperature of 1 keV. The BCG is at a redshift of 0.0338, which is 800 km s^{-1} offset from the median redshift of the member galaxies at 0.0365. We assume that the BCG travels at 800 km s^{-1} relative to the ICM of Abell 1142. Given that the BCG and the orphan CC are offset by 80 kpc in projection, we infer that the orphan CC may have been detached from the BCG for more than 100 Myr. It would accumulate at least $1.2 \times 10^8 M_{\odot}$ cold gas. The upper limit of $1.4 \times 10^8 M_{\odot}$, obtained from the IRAM 30-m observation, indicates that runaway cooling does not occur in the orphan CC, even in the absence of AGN feedback. Furthermore, even if cooling takes place as expected, the ionized warm gas may not be converted into cold molecular gas efficiently. This conversion ineffectiveness may be precisely due to the lack of a galaxy, as warm and cooling gas usually flows onto the galaxy to form molecular hydrogen, catalysed by dust. A follow-up observation of the ionized hydrogen of Abell 1142 would be critical to resolve the scenarios.

With low spatial resolution, Webb et al. (2017) detected $1.1 \times 10^{11} M_{\odot}$ of molecular gas, in the CC cluster SpARCS1049+56 at $z = 1.7$, which they interpreted to be associated with the X-ray peak. The molecular gas, in this case, could have arisen from massive runaway cooling of the nascent ICM (Hlavacek-Larrondo et al. 2020).

However, the separation between the coolest ICM and BCG is only 25 kpc in SpARCS1049+56, for which we expect even less time for cooling than Abell 1142. In fact, Northern Extended Millimeter Array (NOEMA) observations of SpARCS1049+56 revealed, at high resolution, that at least 50 per cent of the molecular gas is associated with the BCG companions, and the rest of the cold gas is in a tidal or ram-pressure tail (Castignani, Combes & Salomé 2020). Therefore, most of the cold gas is not associated with the X-ray peak, and cooling cannot be the dominant mechanism for the formation of its cold gas reservoir.

It is interesting to compare the orphan CC in Abell 1142 and the orphan cloud in Abell 1367 (Ge et al. 2021). Both reside in the nearby Universe and have similar X-ray luminosity ($L_{\text{X, bol}} = 3 \times 10^{41} \text{ erg s}^{-1}$). Multiphase gas from X-ray to molecular cold gas has been detected in the orphan cloud, while the orphan CC is likely to be single phase. One possibility is that the cold gas of the orphan cloud, instead of being formed from cooling, is stripped from its host galaxy. The mixing between this stripped cold gas and the ambient hot ICM has led to the formation of warm ionized gas detected through $\text{H}\alpha$ emission. Another key difference lies in their hot gas metallicity. The orphan cloud has a surprisingly pristine metallicity of $0.14 Z_{\odot}$ (Ge et al. 2021), while that of the orphan CC has a Solar abundance. The measured metallicity of the orphan cloud may have been biased low by its complicated temperature structure.

5 CONCLUSIONS

In this work, we have presented a multi-wavelength study of the nearby cluster Abell 1142, featuring a cluster CC that is not associated with any galaxy and offset from its BCG by 80 kpc. The composition and thermal properties of this orphan CC can provide unique constraints on the enrichment and cooling processes in the ICM. Our findings obtained with *XMM-Newton* and IRAM 30-m observations are summarized below.

(i) The central $r < 25$ kpc of the orphan CC has a prominent Fe abundance peak of ~ 1 solar abundance. Its α/Fe ratio is fully consistent with the solar ratio. Both the metallicity and chemical composition of this orphan CC (with a reduced impact from the innermost atmosphere of the BCG) are in excellent agreement with those observed for typical cluster CCs. This result hints that the stellar mass-loss of the BCG may have a limited contribution to the enrichment of cluster centres. However, the consistent abundance ratios within 1σ error of the orphan CC (0.95 ± 0.28 Solar ratio) and the BCG ISM (0.65 ± 0.28 Solar ratio) mean that the issue remains unresolved.

(ii) Abell 1142 has clearly been through a recent major merger that has disassociated the CC from the BCG and created a bimodal velocity distribution of the member galaxies. The prominent Fe abundance peak, found to be associated with the orphan CC, indicates that major mergers can not easily erase the Fe peak in CC clusters.

(iii) The lack of CO(1-0) and CO(2-1) emission indicates that the orphan CC is not multiphase. Assuming that it has been detached from the BCG for 100 Myr, we expect it to accumulate $1 \times 10^8 M_{\odot}$ molecular gas in H_2 , which is comparable to the upper limit we obtained from the IRAM 30-m observations. An occurrence of runaway cooling in the absence of AGN feedback can be ruled out. The ionized warm gas, if there is any, may not be converted into cold molecular gas efficiently because of the lack of a galaxy.

ACKNOWLEDGEMENTS

The authors thank the anonymous reviewer for their helpful comments on the manuscript. YS and VO acknowledge support by National Science Foundation (NSF) grant 2107711, *Chandra* X-ray Observatory grants GO1-22126X, GO2-23120X, G01-22104X, National Aeronautics and Space Administration (NASA) grants 80NSSC21K0714 and 80NSSC22K0856. GC acknowledges the support from the grant Agenzia Spaziale Italiana (ASI) n.2018-23-HH.0. RvW acknowledges support from the European Research Council (ERC) Starting Grant ClusterWeb 804208.

DATA AVAILABILITY

The data underlying this article will be shared on reasonable request to the corresponding author.

REFERENCES

- Asplund M., Grevesse N., Sauval A. J., Scott P., 2009, *ARA&A*, 47, 481
 Castignani G., Combes F., Salomé P., 2020, *A&A*, 635, L10
 De Propriis R. et al., 2021, *MNRAS*, 500, 310
 E Blackwell A., Bregman J. N., Snowden S. L., 2022, *ApJ*, 927, 104
 Fabian A. C., 2012, *ARA&A*, 50, 455
 Ge C. et al., 2021, *MNRAS*, 505, 4702
 Ghizzardi S. et al., 2021, *A&A*, 646, A92
 Hlavacek-Larrondo J. et al., 2020, *ApJ*, 898, L50
 Jáchym P. et al., 2022, *A&A*, 658, L5
 Kollmeier J. et al., 2019, *BAAS*, 51, 274
 Kraft R. et al., 2022, preprint ([arXiv:2211.09827](https://arxiv.org/abs/2211.09827))
 Leccardi A., Rossetti M., Molendi S., 2010, *A&A*, 510, A82
 Mernier F. et al., 2018, *MNRAS*, 480, L95
 Olivares V., Su Y., Nulsen P., Kraft R., Somboonpanyakul T., Andrade-Santos F., Jones C., Forman W., 2022, *MNRAS*, 516, L101
 Peterson J. R., Kahn S. M., Paerels F. B. S., Kaastra J. S., Tamura T., Bleeker J. A. M., Ferrigno C., Jernigan J. G., 2003, *ApJ*, 590, 207
 Ruppin F., McDonald M., Bleem L. E., Allen S. W., Benson B. A., Calzadilla M., Khullar G., Floyd B., 2021, *ApJ*, 918, 43
 Sarkar A., Su Y., Truong N., Randall S., Mernier F., Gastaldello F., Biffi V., Kraft R., 2022, *MNRAS*, 516, 3068
 Simionescu A., Werner N., Urban O., Allen S. W., Ichinohe Y., Zhuravleva I., 2015, *ApJ*, 811, L25
 Solomon P. M., Barrett J. W., 1991, in Combes F., Casoli F., eds, Proc. IAU Symp. Vol. 146, Dynamics of Galaxies and Their Molecular Cloud Distributions. Kluwer, Dordrecht, p. 235
 Su Y., Buote D. A., Gastaldello F., van Weeren R., 2016, *ApJ*, 821, 40
 Su Y., Nulsen P. E. J., Kraft R. P., Forman W. R., Jones C., Irwin J. A., Randall S. W., Churazov E., 2017, *ApJ*, 847, 94
 Su Y. et al., 2020, *MNRAS*, 498, 5620
 Tacconi L. J. et al., 2018, *ApJ*, 853, 179
 Urban O., Werner N., Allen S. W., Simionescu A., Mantz A., 2017, *MNRAS*, 470, 4583
 Webb T. M. A. et al., 2017, *ApJ*, 844, L17
 Werner N., Urban O., Simionescu A., Allen S. W., 2013, *Nature*, 502, 656

This paper has been typeset from a $\text{\TeX}/\text{\LaTeX}$ file prepared by the author.